Synthetic Wavelength Holography: Snapshot Non-Line-of-Sight Imaging with High-Resolution and Wide Field of View

Florian Willomitzer (florian.willomitzer@northwestern.edu)
Northwestern University
Prasanna Rangarajan
Southern Methodist University, TX
Fengqiang Li
Northwestern University, IL
Muralidhar Balaji
Southern Methodist University, TX
Marc Christensen
Southern Methodist University, TX
Oliver Cossairt
Northwestern University, IL

Article

Keywords: scattering medium, Synthetic Wavelength Holography, imaging system

Posted Date: December 3rd, 2020

DOI: https://doi.org/10.21203/rs.3.rs-84906/v1

Version of Record: A version of this preprint was published at Nature Communications on November 17th, 2021. See the published version at https://doi.org/10.1038/s41467-021-26776-w.

Synthetic Wavelength Holography: Snapshot Non-Line-of-Sight Imaging with High-Resolution and Wide Field of View

Florian Willomitzer[1,*], Prasanna V. Rangarajan[2], Fengqiang Li[1], Muralidhar M. Balaji[2], Marc P. Christensen[2], and Oliver Cossairt[1]

[1]Department of Electrical and Computer Engineering, Northwestern University, Evanston, IL 60208

[2]Department of Electrical and Computer Engineering, Southern Methodist University, Dallas, TX 75205

[*]Correspondence: florian.willomitzer@northwestern.edu

The presence of a scattering medium in the imaging path between an object and an observer is known to severely limit the visual acuity of the imaging system. We present an approach to circumvent the deleterious effects of scattering, by exploiting spectral correlations in scattered wavefronts. Our Synthetic Wavelength Holography (SWH) method is able to recover a holographic representation of hidden targets with high resolution over a wide field of view. The complete object field is recorded in a snapshot-fashion, by monitoring the scattered light return in a small probe area. This unique combination of attributes opens up a plethora of new Non-Line-of-Sight imaging applications ranging from medical imaging and forensics, to early-warning navigation systems and reconnaissance. Adapting the findings of this work to other wave phenomena will help unlock a wider gamut of applications beyond those envisioned in this paper.

Introduction

There are numerous instances of imaging within the physical sciences wherein an opaque barrier (such as a wall) or a scattering medium (such as fog or tissue) impedes direct view of the object. Over the years, many attempts [1–13] have been made to non-invasively recover images of objects obscured from direct view. These techniques are collectively referred to as 'Non Line-of-Sight Imaging' (NLoS) in our work. The problem is enjoying renewed attention due to emerging applications in autonomous navigation, planetary exploration, industrial inspection, and early-warning systems for first-responders [14–23].

Broadly speaking, current approaches to NLoS imaging circumvent the effect of scatter in one of two geometries: discrete scattering events distributed across multiple interfaces such as walls, and continuous scattering within a volume such as fog or tissue. Herein, we introduce a holographic approach - "Synthetic Wavelength Holography" (SWH) - that advances the state-of-the-art in NLoS imaging by exploiting spectral correlations in scattered light to see through any scattering geometry.

We make specific use of the observation that coherent light at two closely spaced wavelengths λ_1, λ_2 traversing near identical geometric paths in a scattering medium, preserves phase information at scales exceeding a 'Synthetic Wavelength' (SWL) $\Lambda >> \lambda_1, \lambda_2$ [24, 25]. We provide experimental evidence corroborating the above claim. Moreover, we establish that the optimal choice of the SWL scales with increasing scatter, and the synthetic phase computed at the distal end of the scattering medium encodes a holographic description of the obscured objects. The mathematical principles underlying the proposed imager concept expand the understanding of light transport in the presence of scatter.

A specific embodiment of the NLoS imaging problem is the task of looking around corners. We use this task to introduce the proposed approach and provide a basis for the comparative assessment with competing approaches. Existing schemes for imaging around corners attempt to recover the obscured scene by either exploiting the finite speed of light ("Time of Flight" *ToF* based techniques [16–19]) or spatial correlations in scattered light ("Memory Effect" *ME* based techniques [20, 25–29]).

ToF based NLoS Imaging techniques recover a surface representation of the hidden scene by probing the scene with a temporally modulated source, and recording the response using fast detectors. The process is repeated across multiple spatial locations (so-called 'virtual sources and detectors' - VS and VD) of an intermediary surface such as a wall or floor that is simultaneously visible to the obscured objects and the NLoS sensor unit. Recent work in the area [16–19] has demonstrated results with cm-scale lateral resolution over a $1m \times 1m \times 1m$ volume, and in select cases providing near real-time reconstructions. The approach, however, is limited by the need for raster-scanning large areas on the intermediary VS/VD surface whose dimensions are comparable to the obscured volume.

The second class of techniques for imaging around corners exploits spatial or angular correlations in scattered light [20, 25–29]. The images of obscured objects recovered using these techniques feature the highest lateral resolution ($< 100\mu m$ at $1m$ standoff), for the smallest probing area on the intermediary VS/VD surface (< few cm). The improved resolution, however, comes at the expense of a highly restricted angular FoV ($< 2°$), as determined by the angular decorrelation of scattered light (Memory Effect [30, 31]). The *ME* does not only limit the FoV, but also (even more severe!) the maximal possible size of the measured object

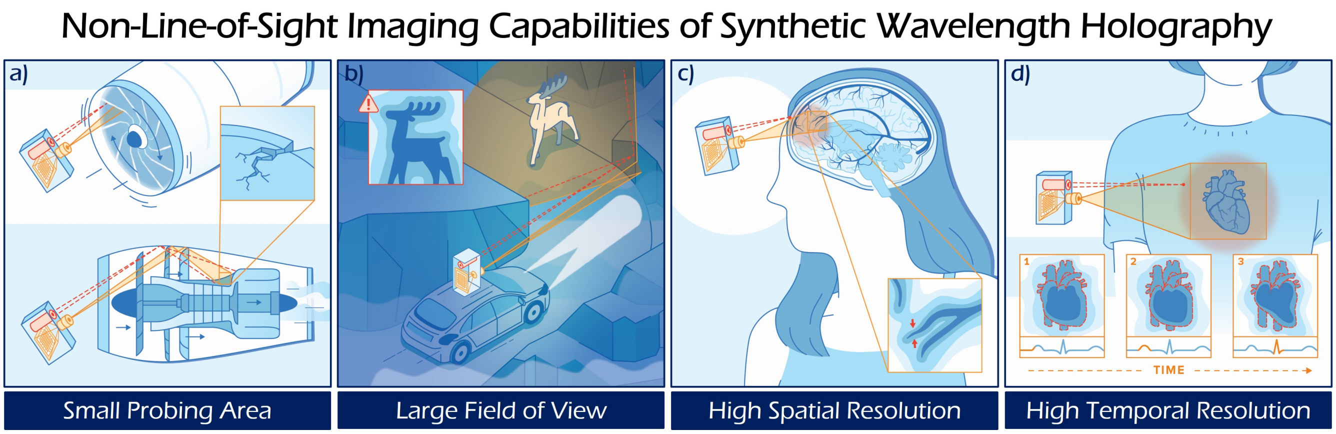

Fig. 1. Imaging objects obscured from direct view using 'Synthetic Wavelength Holography'(SWL). The approach combines four key attributes highlighted in the following NLoS application scenarios: In each example, a scattering surface or medium is used to indirectly illuminate, and intercept light scattered by the hidden objects. a) A small probing area allows to inspect defects in tightly confined spaces, e.g., in running aircraft engines. b) A large FoV allows to measure/detect hidden objects without previous knowledge of their position as, e.g., important when navigating in degraded visual environments. c) High spatial resolution allows for the measurement of small structures, such as non-invasive imaging of brain vessels through the skull. d) High temporal resolution allows to image objects in motion, e.g., to discern cardiac arrhythmia through the chest. The combination of these attributes in a single approach is unprecedented in the current state of the art.

which cannot be larger than the FoV.

The wide disparity in the FoV and resolution of current NLoS Imaging schemes greatly limits their utility. We demonstrate how to recover a truly holographic description of the obscured scene with a high spatial resolution, over a wide field of regard. Our SWH approach exploits *spectral correlations in scattered light* at optical wavelengths λ_1, λ_2 to assemble a hologram of the obscured objects at the SWL $\Lambda = \frac{\lambda_1 \lambda_2}{|\lambda_1 - \lambda_2|}$. The approach combines a unique set of capabilities in providing a degree of versatility that is unmatched by competing NLoS approaches:

- **Small Probing Area** (see Fig. 1a): ToF based NLoS schemes use probing areas ~ $1m \times 1m$. SWH provides the ability to image obscured objects in tightly confined spaces by simultaneously illuminating and observing a small area ($58mm \times 58mm$ in our experiments). Potential applications include inline defect detection and inspection in heavy machinery such as running turbines, and endoscopic imaging applications.

- **Large Field of View** (see Fig. 1b): ME-based approaches produce highly restricted FOVs (< 2° for drywall), while SWH provides the ability to recover holograms of obscured objects over a hemispherical FoV that far exceeds the limited angular extent of the memory effect. Potential applications include the design of early-warning systems in automotive sensing and planetary exploration.

- **High Spatial Resolution** (see Fig. 1c): ToF-based approaches produce low spatial resolutions (~ cm). SWH provides the ability to resolve small features on obscured objects (up to < $1mm$ in our experiments) without requiring prior knowledge of the scattering geometry or attributes of the scattering medium such as the transmission matrix [32, 33]. Potential applications include non-invasive imaging of blood vessels through tissue.

- **High Temporal Resolution** (see Fig. 1d): ToF-based approaches require point-wise raster-scanning, while SWH provides the ability to recover holograms of the obscured object in a snapshot fashion using conventional focal plane array (FPA) technology. This allows to resolve object motion such as sensing cardiac arrhythmia's through the chest, and remotely sensing surface motion of small planetary bodies [34].

The mathematical principles underlying SWH are by no means restricted to the applications discussed above. The approach can be adapted to other NLoS imaging tasks including imaging through deep turbulence, fog and turbid waters, imaging through optically opaque barriers such as the skull, or face identification around corners. The idea of utilizing wavelength diversity to alleviate the effects of unwanted aberrations in the detection of electromagnetic signals has potential applications that go far beyond the original scope of NLoS imaging. We conclude this paper by discussing benefits of applying the SWH principle in a diverse set of application areas such as medical ultrasound, synchrotron X-ray diffraction imaging, and radio astronomy.

Synthetic Wavelength Holography (SWH)

Holographic approaches to imaging, including SWH, exploit the availability of a coherent source for illumination and interferometric sensing. Repeated scattering irreversibly randomizes the interference so that the speckle pattern recorded on the detector bears no resemblance to the macroscopic structure of the object.

However, a small change in the interrogation wavelength produces a largely identical speckle pattern with residual changes in phase that encode the macroscopic structure of the obscured object [24, 25]. We exploit this fact to probe the scattering medium at two closely spaced wavelengths λ_1 and λ_2, and record the emerging speckle fields $E(\lambda_1)$ and $E(\lambda_2)$, as illustrated in Fig. 2a. Computational mixing of

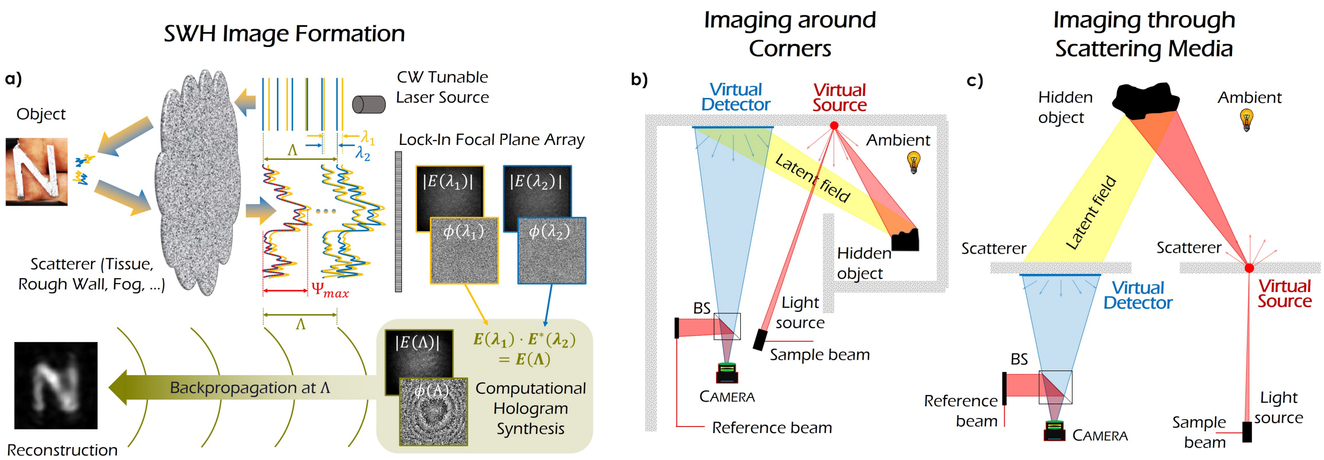

Fig. 2. Schematics of SWH for NLoS imaging around corners and NLoS imaging through scattering media. a) SWH image formation: A CW-tunable laser illuminates the scene at two slightly different wavelength λ_1 and λ_2. Each field $E(\lambda_1)$, $E(\lambda_2)$ is subject to multiple scattering processes in or at the scatterer (which could be wall, tissue, fog,...) and the rough object surface. The introduced maximal pathlength variation Ψ_{max} leads to a complete randomization of $E(\lambda_1)$, $E(\lambda_2)$ when arriving at the detector. However, computational mixing of the speckled fields $E(\lambda_1) \cdot E^*(\lambda_2) = E(\Lambda)$, yields a complex-valued hologram of the object at a 'Synthetic Wavelength' (SWL) $\Lambda = \frac{\lambda_1 \cdot \lambda_2}{|\lambda_1 - \lambda_2|}$. The object is reconstructed by backpropagating $E(\Lambda)$ with the SWL Λ. b) and c) Schematic setups for NLoS imaging around corners (b) and NLoS imaging through scatterers (c) with the SWH principle: The sample beam illuminates a spot on the wall/scatterer (the 'Virtual Source' VS), which scatters light towards the obscured object. A small fraction of the light incident on the object is scattered back to the wall/scatterer where it hits the 'Virtual Detector' (VD). The VD is imaged by the camera, meaning that the synthetic hologram is captured at the VD surface.

the fields $E(\lambda_1) \cdot E^*(\lambda_2) = E(\Lambda)$, yields a complex-valued hologram of the object at the SWL $\Lambda = \frac{\lambda_1 \cdot \lambda_2}{|\lambda_1 - \lambda_2|}$ (see Fig. 2a). For closely spaced optical wavelength λ_1 and λ_2, the SWL is orders of magnitude larger than λ_1, λ_2 so that the computationally recovered field $E(\Lambda)$ is robust to the deleterious effects of scattering. An image of the hidden object can be retrieved by numerical backpropagation of $E(\Lambda)$ at the SWL Λ, as illustrated in Fig. 2a.

The strikingly simple and computationally inexpensive strategy described above can significantly improve the visual acuity of imaging systems confounded by scatter. The computational immunity to scatter afforded by the existence of spectral correlations, relies only on the wave nature of light. As a consequence, the principles underlying SWH can be readily extended to other wave phenomena such as radio waves and acoustic waves (ultrasound).

Experimental Validation of SWH for Different NLoS Imaging Techniques

'Looking around corners'.

We use the scene arrangement depicted in Figure 2b to elucidate the SWH principle and demonstrate the ability to record holograms of objects beyond the line-of-sight. The portions of the wall designated VS and VD are used to indirectly illuminate the hidden object, intercept the scattered latent field and relay it towards a focal plane array (FPA) that records the scattered field. Details of the image acquisition process and the imaging apparatus are provided in the methods section and the supplementary material. An image of the obscured object is recovered as explained above, i.e., by mixing the scattered optical fields $E(\lambda_1)$ and $E(\lambda_2)$ and playing back the assembled synthetic wavelength hologram $E(\Lambda)$ with the SWL Λ. The use of tunable lasers allows us to accommodate a variety of scattering scales by freely tuning the SWL over a wide interval ranging from hundreds of μm to hundreds of m.

Figures 3a-e illustrate the phase of the computationally assembled synthetic wavelength hologram, for a specific set of SWLs. In each case, we are able to recover optical phase information, despite the pronounced scattering at the wall and object surface. The outcome of back-propagating the synthetic holograms is shown in Figs. 3f-j. The results confirm the ability to recover an image of a small object, character 'N' (dimensions $15mm \times 20mm$, see Fig. 3q) that is obscured from view. Furthermore, the *phase information* encapsulated in the synthetic hologram allows us to locate the hidden object within the obscured volume (illustrated in Fig. 5 and described later).

Figures 3f-j confirm that the resolution of the reconstruction improves with decreasing SWL Λ. This behavior is in agreement with results from classical holography. It implies that the synthetic wave, although a computational construct, has distinct characteristics that it shares with a physical wave at the respective wavelength Λ. The notion is corroborated in Fig. 3k-p wherein we attempt to localize a point-source obscured from view. It is observed that a diffraction limit may be ascribed to the computationally assembled synthetic hologram, in much the same manner as classical holography. The radius of the resulting 'Synthetic Diffraction Disc' is given by:

$$\delta x \approx \Lambda \frac{z}{D} \quad , \qquad \textbf{(1)}$$

where D is the diameter of the probing area at the VD, and z is the propagation distance to the object. The ratio $D/2z$ defines the numerical aperture of the computational NLoS-imager. In the present example, a lateral resolution limit of $\delta x = 800\mu m$ is reached for a SWL of $\Lambda = 280\mu m$. Details of the experiment are included in the methods section.

The expression for the resolving power of SWH disclosed

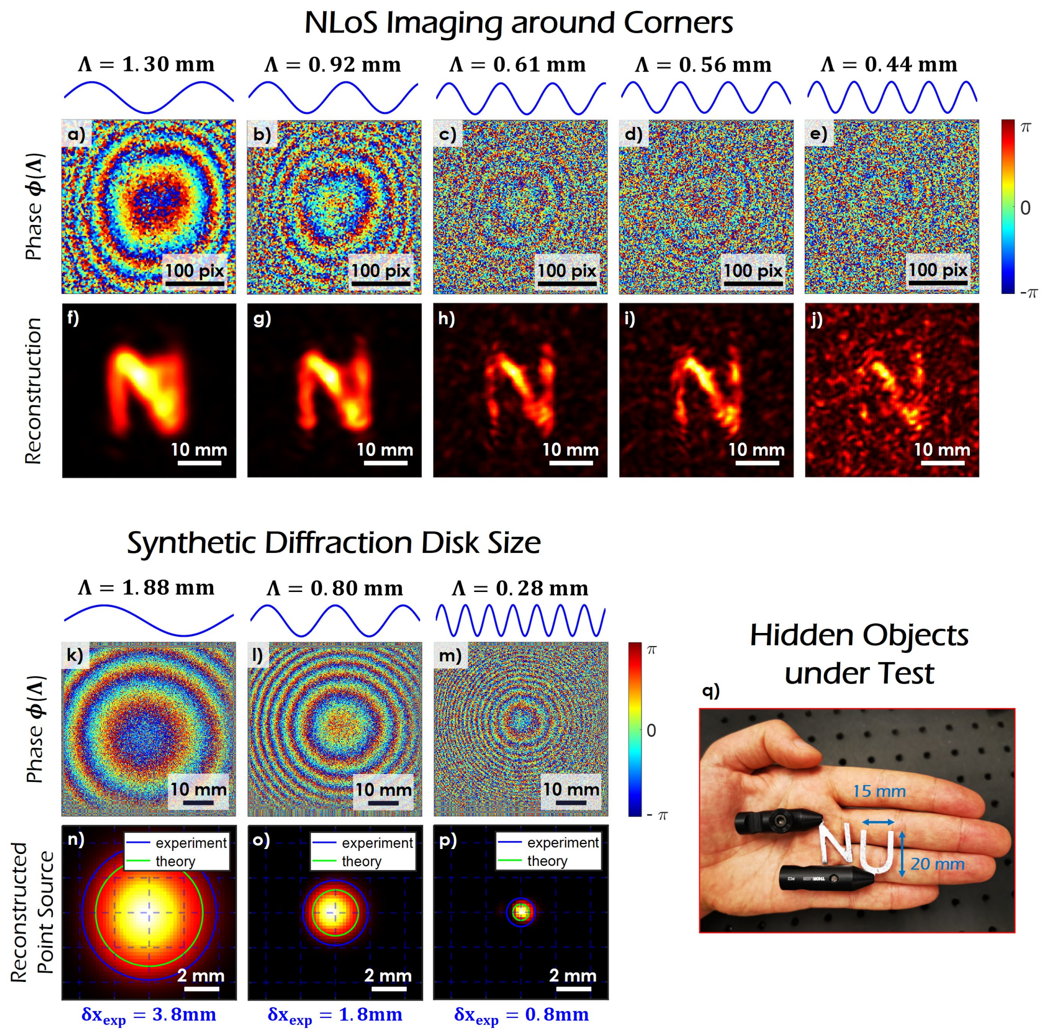

Fig. 3. Experimental results for imaging around corners with SWH. a)-j) Imaging the character 'N' ($\sim 15mm \times 20mm$) at five different SWLs. a)-e) The phase of the synthetic holograms at the VD surface. f)-j) Respective reconstructions. The resolution of the reconstructions increases with decreasing SWL. However, the speckle-artifacts increase due to the decorrelation of the two optical fields at λ_1 and λ_2. k)-p) Reconstruction of an obscured point source for three different SWLs. k)-m) Phase of the synthetic holograms at the VD surface. n)-p) Reconstruction of the 'synthetic diffraction disc'. As in classical optics, the disc size varies linearly with the wavelength (in this case the SWL). The experimental value is close to the theoretical expectation. For p), the point source is reconstructed with sub-mm precision. q) Image of the targets used in the experiments of this paper: Two characters 'N' and 'U' with dimensions $\sim 15mm \times 20mm$ (plus black mountings).

in Eq. 1, suggests that the resolution may be indefinitely improved by reducing the SWL Λ. This however is not the case. For increasingly small values of Λ, the reconstructions exhibit speckle-like artifacts (see e.g. Figs 3f-j). The artifacts are attributed to a loss in the spectral correlation of the scattered fields observed at λ_1, λ_2. The physical origins of this decorrelation are well documented in literature [31, 35–46]. The supplementary material includes a derivation for the specific case of 'looking around corners'.

'Looking through scatter' .

The notion of exploiting spectral correlations for NLoS imaging is by no means restricted to the 'looking around corners' problem. To highlight the versatility of the SWH approach, we recover holograms of objects embedded beneath a scattering medium, as illustrated in the schematic of Fig. 2c. In a first set of measurements, we image the small character 'U' (dimensions $15mm \times 20mm$, see Fig. 3q) through a 220-grit diffuser (Fig. 4a top). The holographic reconstructions are displayed in Fig. 4b-e. As the SWL falls below $300\mu m$, we begin to notice 'synthetic speckle' artifacts in the reconstructed image, suggesting that wavelength separation has increased to the point that the captured optical holograms are uncorrelated for this specific scene.

In a second set of experiments, we swap the diffuser in the imaging path with a $4mm$ thick milky white plastic plate. Figure 4a illustrates the impact of pronounced multiple scattering on the visibility of a checkerboard that is viewed through the plastic plate and the 220 grit ground glass diffuser. It is clear from the results of Figs. 4f-i that we are able to reconstruct the character 'U' for SWLs $\Lambda \geq 360\mu m$. The results confirm the ability to recover image information at visibility levels that are far below the perceptual threshold, due in large part to scattering.

A comparison of the reconstruction results for the plastic plate and the diffuser reveals only a marginal change in the smallest achievable SWL, as we switch from thin scattering surfaces to thick scattering media. The implications of this

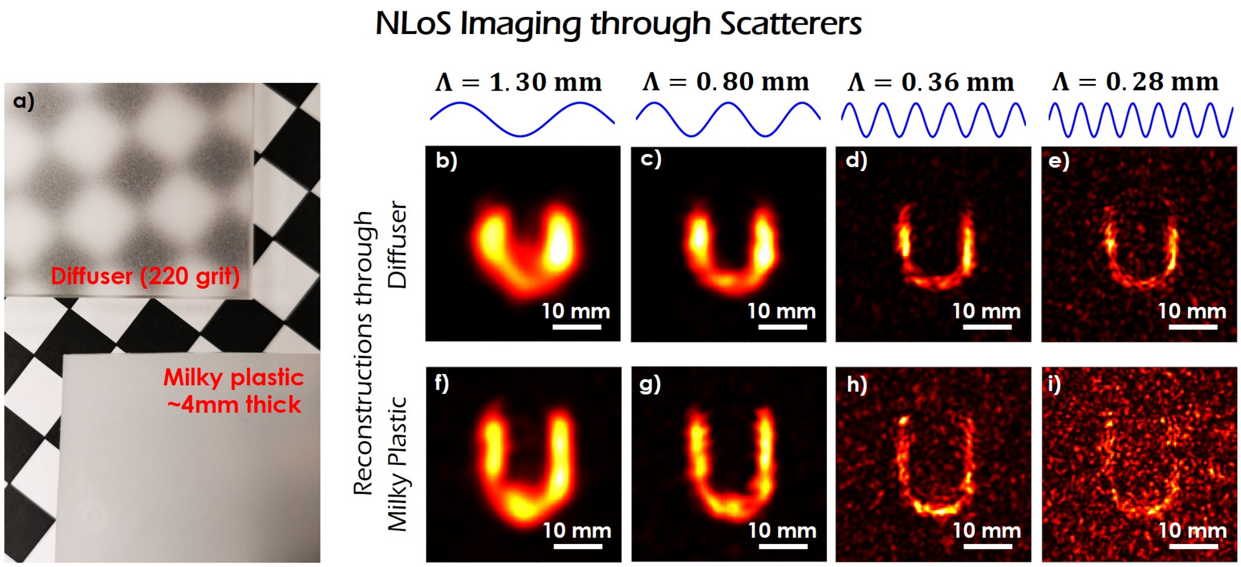

Fig. 4. Experimental results for imaging through scattering media with SWH. A schematic of the experimental setup is available in Fig. 2c. a) Scatterers obscuring the object: A 220 grit ground glass diffuser and a milky white plastic plate of $\sim 4mm$ thickness, both placed $\sim 1cm$ over a checker pattern to demonstrate the degradation in visibility. b)-e) Reconstructions of measurements taken through the ground glass diffuser. f)-i) Reconstructions of measurements taken through the milky plastic plate. The character can be reconstructed with impressive quality. The larger OPD in the plastic plate leads to greater decorrelation if the SWL is decreased.

observation are best understood by recognizing that the visibility of ballistic light paths decays exponentially with the propagation distance through a scattering volume (in accordance with Beer's law [47]).

Synthetic Pulse Holography.

The principles underlying the proposed SWH concept can be extended to include multiple illumination wavelengths. The resulting spectral diversity is expected to yield an improvement in the longitudinal resolution, in much the same manner as Optical Coherence Tomography (OCT) [49–52] and White-Light Interferometry (WLI) [53, 54]. However, unlike OCT and WLI, we do not need to match the power and pathlengths in the two inteferometer arms.

To demonstrate the improvement in longitudinal resolution afforded by the use of multiple SWLs, we computationally section a three-dimensional NLoS scene comprised of two previously introduced characters 'N' and 'U' (both $15mm \times 20mm$) that are offset in depth by $\Delta z \approx 33mm$. Using a single SWL of $\Lambda = 800\mu m$ it is possible to separate the characters laterally, but with limited longitudinal resolution, as shown in Figs. 5b-e. Since we have access to the complex-

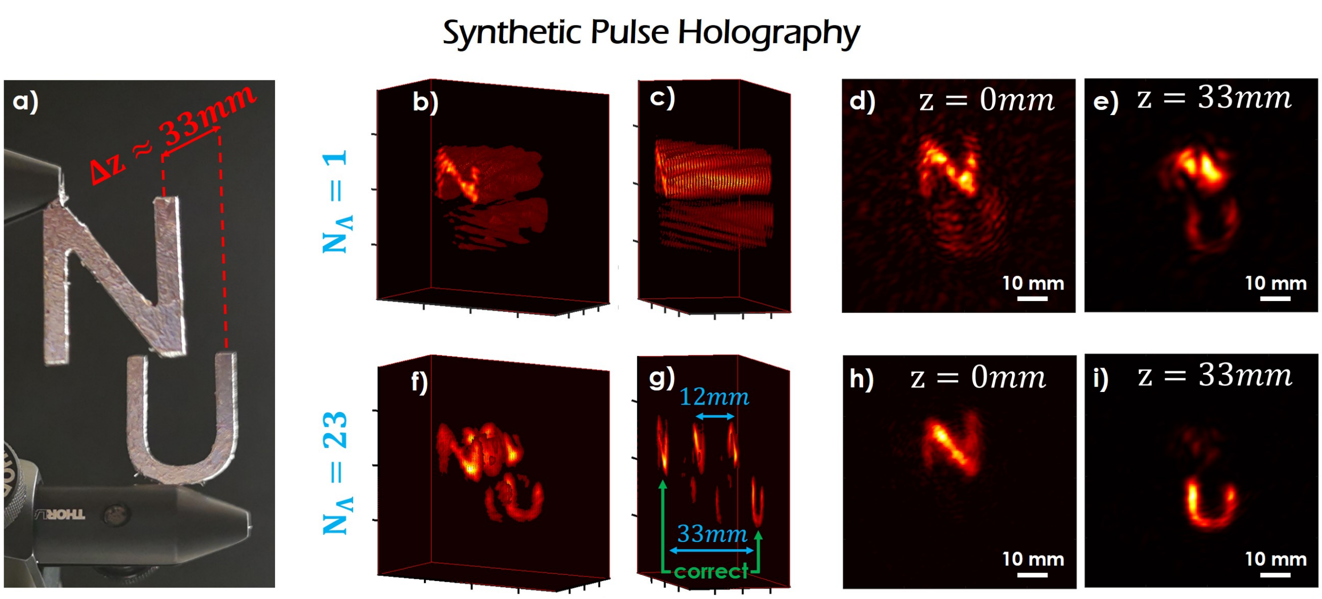

Fig. 5. Experimental Results for the generation of a 'synthetic pulse train' with SHW. a) Target, consisting of two characters with a longitudinal separation of $33mm$. b)-e) Reconstruction of the characters, using only $N_\Lambda = 1$ SWL ($\Lambda = 0.8mm$). Due to the properties of holographic backpropagation, a separation of the characters in depth is not possible. f)-i) Reconstruction, calculated from coherent superposition of the backpropagated fields at $N_\Lambda = 23$ SWLs. Letters are separable. The pulse distance of the synthesized pulse train can be seen in (f) and (g).

valued field information at each synthetic wavelength, it is possible to improve the longitudinal resolution of SWH by coherently combining the synthetic fields recorded at a multitude of synthetic wavelengths ($N_\Lambda = 23$ in Fig. 5). The computational approach mimics scene interrogation by a periodic pulse train, and the replicas observed in the reconstructions of Fig. 5f and 5g are consistent with the periodicity of the computationally engineered pulse train (frequency offset of $25GHz$ corresponding to a depth ambiguity of $12mm$). An unambiguous measurement range in excess of $33mm$ requires a frequency increment of ~ $1GHz$, which has been experimentally verified with our laser system as well. It is anticipated that locking the tunable laser source to a frequency ruler such as a frequency comb will further improve the longitudinal resolution, due in large part to the precise phase relationship between the individual comb teeth [55–57].

NLoS Wavefront Sensing.
The experiments in SWH described thus far have restricted attention to recovering objects obscured by scattering media. However, the principle underlying SWH, namely spectral correlations in scattered light, is rather general and has broader appeal. We demonstrate the ability to recover residual phase variations in the wavefronts emerging from a volumetric scattering sample. The data for this experiment where captured by the authors of [48] without the original intention to be used for our approach. Details of the experimental apparatus are available in Kadobianskyi et.al. [48]. The authors recorded speckle fields emerging from $720\mu m$ (Fig. 6a,b) and $1080\mu m$ (Fig. 6d,e) thick scattering samples with a scattering mean free path of $90\mu m$. In each case, the sample is interrogated by a quasi-monochromatic collimated beam at 801 equally spaced wavelength steps spanning the range $690nm$ to $940nm$. By computationally mixing speckle holograms recorded at adjacent wavelengths, we are able to identify a hologram at the SWL of $\Lambda = 2.1mm$. Results from the experiment are shown in Fig. 6. The phase of the synthetic hologram exhibits a distinct spatial structure that is consistent with the observation of interference fringes due to interreflections between the laser aperture and a polarized beam splitter in the illumination path; according to the authors of [48]. It is worth emphasizing that the wavefront sensing approach described above, relies only on the scattered light paths as the ballistic paths are expected to be extinguished by factors of 10^{-8} and 10^{-12} in the $720\mu m$ and $1080\mu m$ sample respectively.

Discussion and Conclusion

The present work combines the expressive power of holography with spectral correlations in scattered light to tackle the challenging problem of NLoS imaging. Using only a small probing area ($58mm \times 58mm$ in our experiments), we are able to recover a high-resolution (up to $< 1mm$) holographic representation of obscured objects, over a hemispherical FoV. The technique is robust enough to accommodate different NLoS imaging scales (looking around corners to looking through fog) and scattering geometries (scattering at multiple interfaces to volumetric scatter).

The use of continuous wave sources at different wavelengths allowed us to bypass the need for ultrafast sources (picosecond pulses) and fast detectors (SPAD detectors, streak cameras), both of which are routinely employed in competing NLoS approaches. The use of full-field focal plane arrays additionally allowed us to bypass the need for raster scanning in ToF based NLoS schemes.

The SWH approach, however, is not without limitations, chief of which is the inability to recover phase information when the optical fields at the two wavelengths $E(\lambda_1)$ and $E(\lambda_2)$ are uncorrelated. It manifests as speckle-like artifacts in the reconstructed images at the SWL ('synthetic speckle'), such as those observed in Figs. 3j and 4i. The problem may be avoided by judicious selection of the interrogation wavelengths λ_1, λ_2. It is observed that phase fluctuations ex-

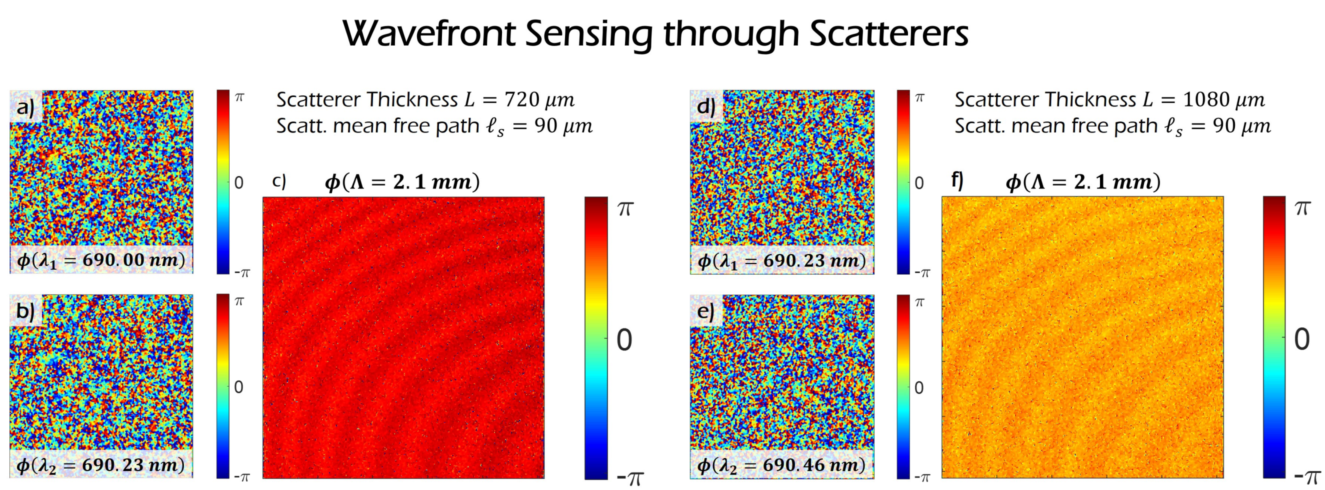

Fig. 6. Experimental Results for Wavefront sensing through scatterers with SWH. The data for this experiment where captured by the authors of [48] without the intention to be used for our approach. Nevertheless, our SHW reconstruction mechanism is able to recover residual phase variations in speckled wavefronts emerging from volumetric scattering samples. a) and b) Scattered (speckled) phasemaps after the volumetric scattering sample with thickness $L = 720\mu m$ and scattering mean free path $\ell_s = 90\mu m$ for two different wavelengths $\lambda_1 = 690.00nm$ and $\lambda_1 = 690.23nm$. c) Calculated synthetic phase map for $\Lambda = 2.1mm$. d)-f) Same experiment with scatterer of different thickness ($L = 1080\mu m$) and optical wavelengths $\lambda_1 = 690.23nm$ and $\lambda_1 = 690.46nm$.

ceeding the SWL may be unambiguously recovered if the largest wavefront error Ψ_{max} introduced during light transport through the scattering scene fulfills a Rayleigh Quarter Wavelength criterion (RQWR [58]) for the SWL, i.e.,

$$\Psi_{max} \leq \frac{\Lambda}{4} \tag{2}$$

The wavefront error Ψ_{max} represents the worst-case spread in the physical lengths of scattered light paths that share a common source location, object location and detector pixel. For surface scattering processes, the spread in path lengths is limited by $2\sigma_h$, where σ_h represents the RMS surface roughness (see Eq. 40 in supplementary material). This is demonstrated experimentally in Fig. 4b-e. Using knowledge of the surface roughness of the 220 grit diffuser and the experimental geometry, we estimate Ψ_{max} to be $65\mu m$. Speckle artifacts are observed when Λ approaches $4\Psi_{max}$, consistent with the RQWR.

The supplementary material puts forth mathematical arguments supporting the existence of RQWR (Eq. 2) for a single realization of a scattering surface (see Section 1.6). The analysis shows how the RQWR fundamentally limits performance of a large class of NLoS imagers, including ToF techniques. Furthermore, the analysis may be generalized to include volumetric scatter by adopting a diffusive approach to light propagation [45]. It is observed that the spread in path lengths as determined by the ratio of the squared thickness of the medium L^2 to the transport mean free path ℓ^*, plays a role analogous to the RMS roughness σ_h of scattering surfaces.

The principal distinction between scattering at discrete interfaces such as walls and continuous scattering through a volume, lies in the scale of wavefront error Ψ_{max}. For instance, the typical wavefront error Ψ_{max} for 'imaging around corners' is less than 1 millimeter, several centimeters for imaging through tissue, and many meters for long-range imaging through fog. It is expected that diffusive scatter over long propagation distances will severely limit the maximal achievable resolution. In the specific case of imaging through fog, we anticipate that the time-gating ability of FMCW LiDAR [59] may be combined with SWH to see farther with a higher resolution than is otherwise possible. In the case of imaging through tissue, it is anticipated that ultrasound focusing aids may be combined with SWH to see farther into the brain with a higher resolution than is currently possible.

The notion of SWH as demonstrated in this paper has a broad range of applications including imaging through obscurants, fog, smoke, tissue, bone, face detection around corners, or 'pseudo-endoscopic' defect detection of mechanical assemblies during operation. These applications largely restrict attention to optical carrier frequencies. However, the true potential of our approach can be unlocked by transferring the notion to other wave phenomena. For instance, we envision the possibility of adapting the SWH principle to ultrasound imaging of biological features embedded deep within layers of tissue. Another example is coherent X-ray diffraction imaging of specimens embedded in thick, inhomogeneous samples. In both the examples, SWH has the potential to decouple the resolution of the reconstruction (determined by the 'Synthetic Frequency') from the penetration depth (determined by the carrier frequency). We also envision the use of SWH in repurposing radio antenna arrays (e.g., the VLA) for space-based astronomical imaging at microwave and radio frequencies through dense atmosphere, and possibly below the surface of a planet for remote geological exploration. Using photonic mixers driven by continuous wave laser sources, it may be possible to simultaneously probe both optical reflectance and spectroscopic information of specimens by sensing THz synthetic wavelengths with optical detection techniques coupled together with direct sensing of THz electromagnetic signals. Moreover, we believe that the SWH concept has huge potential for Material Science, may it be to see deeper through materials or for the precise analysis of inhomogeneous or multi-layered structures.

There is much to be gained from exploiting spectral correlations in coherent light transport. Examining the SWH approach through the lens of Gabor holography provides newer insights into its operation and scope. Gabor originally conceived holography as a two-step process that involved recording an electron wave hologram and subsequently replaying it via optical diffraction. SWH can be interpreted as a generalization of Gabor's original analysis/synthesis technique, with an additional computation step. We hope that this novel view of SWH will help usher a diverse array of new research directions, in much the same manner as the invention of holography did decades ago.

Methods

Formation of a synthetic wavelength hologram. The wavefront aberration correction step adopted in SWH draws inspiration from multi-wavelength interferometry on rough surfaces [35–37]. The process illustrated in the right half of Fig. 2a involves recording speckle fields $E(\lambda_1), E(\lambda_2)$ at two closely spaced illumination wavelengths. Due to the stochastic nature of light scattering, the phase $\phi(\lambda_1), \phi(\lambda_2)$ of each field separately is completely randomized and bears no resemblance to the macroscopic structure of the object. If however, the illumination beams at the two wavelengths originate from the same source position (such as from a single fiber) and the inhomogeneities in the scattering medium are quasi-static, then the fields incident on the detector are highly correlated. This is because the light at the two wavelengths *traverses nearly identical ray paths and experiences nearly identical path length fluctuations*. This assumption and observation forms the basis of our computational approach to accommodating scattering where we correlate the complex-valued fields to recover the synthetic hologram $E(\Lambda) = E(\lambda_1)E^*(\lambda_2)$, with $\Lambda = \frac{\lambda_1\lambda_2}{|\lambda_1-\lambda_2|}$. It can be shown (see supplementary material) that the residual phase fluctuations in the synthetic hologram, given by $\phi(\Lambda) = \phi(\lambda_1) - \phi(\lambda_2)$, preserves phase variations at scales equal or larger than the SWL Λ, and is robust to speckle artifacts. However, the magnitude of the SWH, given by $|E(\Lambda)| = |E(\lambda_1)| \cdot |E(\lambda_2)|$, still exhibits speckle artifacts (see e.g. Fig. 2a).

Interferometer design and lock-in detection of the synthetic hologram. In practice, poor signal-to-background or signal-to-noise ratios, or both, can limit our ability to measure objects at the smallest possible SWL that is defined by the RQWR (Eq. 2). Interferometric approaches exploiting *frequency heterodyning* have particularly advantageous properties with respect to this problem. The principal benefit of adopting these approaches to record holograms is the ability to exploit the heterodyne gain [60] afforded by the use of a strong reference beam, whose baseband optical frequency is slightly detuned from the frequency of light in the object arm. The difference in frequency ν_m is chosen in the RF frequency range ($3kHz$ for our experiments) and realized by using a cascade of acousto-optic or electro-optic modulators (AOM or EOM). Figs. 4 a and b in the supplementary material depict the two interferometer designs that we use to acquire the holograms at the two optical wavelengths. Each design is an adaptation of a Michelson Interferometer, and incorporates a small difference ν_m in the baseband frequency of light in the two arms of the interferometer. It is emphasized that the RF modulation frequency ν_m is *fully decoupled* from the choice of SWL (and therefore from the resolution of our method!), and can be chosen independent of the SWL.

A Lock-In Focal Plane Array camera (LI-FPA) [61] capable of synchronously demodulating the received irradiance at each detector pixel, is operated to detect the RF frequency ν_m. The process directly yields the interferogram at the SWL Λ. The method avoids the need for time consuming raster scanning as necessary in ToF-based techniques, and phase-shifting of the optical signal. It also vastly improves the Signal-to-Background ratio of our measurements by suppressing the unmodulated ambient illumination. The Heliotis C3 LI-FPA [61] used in our experiments yields a $300 \times 300\ pix$ image per measurement. The exposure time of each measurement is $t_{exp} = 23ms$ corresponding to 70 cycles of the RF frequency $\nu_m = 3kHz$. Two independently tunable narrow linewidth CW lasers (Toptica DFB pro $855nm$) are used to illuminate and interrogate the scene. The center wavelength of each laser is $855nm$, and the maximum tuning range is ~ $2.6nm$. This allows us to achieve SWLs $\Lambda \gtrapprox 300\mu m$, corresponding to a beat frequencies $\lessapprox 1THz$.

The holograms in our proof-of-principle experiments were recorded using two specific heterodyne interferometer architectures: a Dual-Wavelength Heterodyne Interferometer (Fig. 4 a in the supplementary material), and a Superheterodyne Interferometer (Fig. 4 b in the supplementary material). The Dual-Wavelength Heterodyne Interferometer is preferred when light loss in the interferometer should be minimized, which is important for many NLoS applications. Light from the two lasers operating at λ_1, λ_2 are coupled together, before being split into the reference and sample arm. The reference arm is additionally modulated by $\nu_m = 3kHz$, using a cascade of two fiber AOM's. During acquisition, each laser is shuttered independently and the lock-in camera records the holograms at the two optical wavelengths, in a time-sequential manner. The LI-FPA provides two images: In-Phase (I) and Quadrature (Q), each of which represents the real and imaginary parts of the speckle fields incident on the image sensor. The expression for the I- and Q-images recorded by the LI-FPA for the wavelength λ_n is:

$$\begin{aligned} I_I(\lambda_n) &= A_n \cos(\phi(\lambda_n)) \\ I_Q(\lambda_n) &= A_n \sin(\phi(\lambda_n))\ , \end{aligned} \tag{3}$$

where A_n is the amplitude at λ_n and $\phi(\lambda_n)$ is the difference in the phase of light in the object and reference arms. Please note that Eq. 3 omits any reference to spatial locations, in the interest of clarity. Subsequently, the synthteic hologram $E(\Lambda)$ is assembled as follows:

$$\begin{aligned} E(\Lambda) &= [I_I(\lambda_1) + iI_Q(\lambda_1)] \cdot [I_I(\lambda_2) + i \cdot I_Q(\lambda_2)]^* \\ &= A_1 A_2 \exp(i \underbrace{(\phi(\lambda_1) - \phi(\lambda_2))}_{\phi(\Lambda)}) \end{aligned} \tag{4}$$

An attractive feature of the time-sequential approach to hologram acquisition described above is that it does not require the use of two tunable lasers. Identical results can be achieved with one laser that is tuned between the two measurements. Possible extensions include: one tunable and one fixed wavelength laser, and one fixed wavelength laser that is split in two arms, one of which includes an additional frequency modulator.

Unfortunately, the simplicity of the time-sequential approach comes at the expense of increased sensitivity to ob-

ject motion between measurements, and time-varying fluctuations in the environmental conditions. Increased robustness to these fluctuations is afforded by the Superheterodyne Interferometer design, wherein light from both lasers is used to simultaneously illuminate the target and scene. A possible realization is shown in Fig. 4b of the supplementary material: each laser beam is split into two arms, where one of which is independently modulated with an AOM. The RF drive frequencies for AOMs 1A and 1B (see Fig. 4 b in the supplementary material) are identically set to ν_{AOM1}, but include a phase offset $\Delta\varphi_{AOM}$ that is user controlled. Light leaving the two AOMs is combined and modulated with a third AOM (frequency ν_{AOM2}), which produces the desired modulation frequency $\nu_m = \nu_{AOM1} - \nu_{AOM2} = 3kHz$. The expression for the I- and Q-images (In-Phase and Quadrature) recorded by the LI-FPA after locking in at ν_m are:

$$
\begin{aligned}
I_I(\lambda_1,\lambda_2) &= A_1\cos(\phi(\lambda_1)+\Delta\varphi_{AOM}) + A_2\cos(\phi(\lambda_2)) \\
I_Q(\lambda_1,\lambda_2) &= A_1\sin(\phi(\lambda_1)+\Delta\varphi_{AOM}) + A_2\sin(\phi(\lambda_2))
\end{aligned}
\tag{5}
$$

The synthetic hologram $E(\Lambda)$ is assembled by calculating:

$$
\begin{aligned}
&I_I^2 + I_Q^2 \\
&\quad = A_1^2 + A_2^2 + A_1A_2\cos(\underbrace{\phi(\lambda_1)-\phi(\lambda_2))}_{\phi(\Lambda)} + \Delta\varphi_{AOM})
\end{aligned}
\tag{6}
$$

The synthetic phase map is eventually recovered from the interferograms recorded with three or more phase shifts $\Delta\varphi_{AOM}$ introduced between measurements. It should be emphasized that the use of two tunable lasers is also not a prerequisite for this approach. Identical results can be achieved with one fixed and one tuned laser, or similar combinations discussed above. The principal benefit of the Superheterodyne approach is the robustness to environmental fluctuations and object motion. However, it requires an additional AOM and fiber splitters that significantly reduce the available output power compared to the Dual Wavelength Heterodyne Interferometer discussed previously. The loss of power presents light throughput challenges for NLoS experiments that are intrinsically light starved.

In practice, there exists a trade-off between light throughput and robustness to environmental fluctuations, which depends on a multiple factors including stand-off distance, reflectivity of the involved surfaces, and laser power.

Reference beam injection with reduced radiometric losses. The reference beam required for interferometric sensing of the speckle fields at the optical wavelengths is directed towards the lock-in FPA. In one possible embodiment, a *lensed fiber needle* (WT&T Inc.) positioned in the front focal plane of the imaging optic (see Fig. 4 f in the supplementary material) produces a near planar reference beam on the FPA. The use of a lensed fiber provides two distinct advantages over a beam-splitter: (1) the imaging optic can be directly threaded to the camera (eliminates the need for inserting beam splitter between optic and sensor) and easily swapped during operation, and (2) improved light throughput (see Tab. 1).

Light Loss in:	Reference Beam	Sample Beam
Lensed Fiber Needle	~ 30%	~ 0%
50/50 Beam Splitter	~ 50%	~ 50%

Table 1. Light loss at combination of reference and sample arm: Lensed fiber needle vs. conventional 50/50 beam splitter

Experimental setup and image formation for reflective NLoS imaging ('looking around corners'). The experimental apparatus schematically displayed in Fig. 2b, and shown in Fig. 4 c of the supplementary material is used to demonstrate the ability of SWH to discern objects obscured from view, in this case a cutout of the character 'N' with dimensions ~ $20mm \times 15mm$. The size of the object was deliberately chosen to be smaller than the typical size of a resolution cell (~ $2cm$) in competing wide-field ToF-based approaches. The disadvantage when using a small object is that it emits less light than the background. The problem is additionally compounded by the limited laser power in the object arm (about $30mW$). In an effort to bypass these engineering limitations, we glued a thin sheet of silver foil to the sandblasted (280 grit) surface of the object 'N' and repeated the process for the VS surface. An image of object 'N' under ambient light can be seen in Fig. 3q. The fields reflected by these materials are fully developed speckle patterns. The VD wall surface is constructed from a standard dry-wall panel that has been painted white (Beer Eggshell paint).

Our approach to reflective NLoS imaging relies on the availability of an intermediary scattering surface (such as the wall in Fig. 2b) that serves to indirectly illuminate the obscured target and intercept the light scattered by the target. Accordingly, the intermediary surface may be viewed as a Virtualized Source (VS) of illumination and a Virtualized Detector (VD) for the obscured object.

Laser light from the physical source (at wavelengths λ_1 and λ_2) is directed towards the VS surface using a focusing optic. This light is scattered by the VS surface so as to illuminate the obscured object with a fully developed objective speckle pattern. A fraction of the light incident on the obscured object is redirected towards the VD surface. A second scattering event at the VD surface directs a tiny fraction of the object light towards the collection aperture, and subsequently the LI-FPA. The speckle fields impinging on the LI-FPA are synchronously demodulated to recover the real and imaginary parts of the holograms at the optical wavelengths λ_1 and λ_2. Each of these holograms is additionally subject to diffraction due to the finite collection aperture. However, the diffraction effects are observed at optical wavelengths and have little impact on the SWL Λ. After assembling the synthetic hologram, the hidden object can be reconstructed by backpropagating the synthetic hologram, using a propagator (Free-Space propagator) at the SWL Λ. In the shown experiments, we used an angular spectrum propagator.

Figure 3 includes the result of processing the NLoS measurements acquired using the experimental setup of Fig. 2b. The measurements were captured at different SWLs ranging from $280\mu m$ to $2.6mm$. Figure 3 shows five exemplary results for $\Lambda = 1.30mm$, $\Lambda = 920\mu m$, $\Lambda = 610\mu m$, $\Lambda = 560\mu m$ and $\Lambda = 440\mu m$. The phase of the synthetic hologram associated with each SWL is shown in Fig. 3 a-e. The phasemaps have been low-pass filtered with kernel size $\approx \Lambda$ for better visualization.

As discussed previously, the reconstruction resolution improves with decreasing SWL. However, decreasing the SWL leads to an increased spectral decorrelation of the speckle fields at the two optical wavelengths. The decorrelation manifests as excessive phase fluctuations in the SWH, which in turn produces increased speckle artifacts in the reconstructed images. The problem can be mitigated (to an extent) by exploiting speckle diversity at the VS, specifically by averaging over multiple speckle realizations of the virtualized illumination. In our experiment, we realized the speckle diversity by small movements of the VS position. The image insets in Figure 3f-j represent the result of incoherent averaging (intensity-averaging) of the backpropagated images, for 5 different VS positions. The improvement in reconstruction quality comes at the expense of increased number of measurements, but not unlike competing ToF-based approaches (e.g. > 20.000 VS positions are used in [17]). The distinction is that we need far fewer images. We conclude our discussion by observing that for static objects, the reconstruction quality may be further improved by increasing the number of VS positions used to realize speckle diversity.

Synthetic diffraction discs and lateral resolution. As seen in Figs. 3f-j, the resolution of the NLoS reconstruction improves with decreasing SWL Λ. This behavior is in complete agreement with results from classical holography. The diffraction limited resolution (minimum resolvable spot radius δx) of SWH can be quantified using Eq. 1, which succinctly captures the relationship between the SWL Λ and the highest resolution that can be achieved. A smaller SWL is clearly desirable since it leads to higher resolution *or* allows for a smaller VD surface (probing area) while keeping the resolution constant. We experimentally validate the above claim (and Eq. 1) by localizing a point-like source in the hidden volume, using a VD diameter of only $D = 58mm$. An exposed fiber connector positioned $z = 95mm$ behind the VD surface serves as a point-source. Holograms at the VD surface acquired with multiple optical wavelengths are processed to recover a multitude of synthetic holograms, each of which is digitally replayed to recover an image of the point-source. The experimentally observed spot sizes or 'synthetic diffraction discs', shown in Figs 3n-p, are consistent with theoretical predictions (red circles, calculated from Eq. 1), and increase with increasing SWL. For a SWL of $280\mu m$, we are able to achieve sub-millimeter resolution around the corner.

Experimental setup and image formation for transmissive NLoS imaging. The experimental apparatus schematically displayed in Fig. 2c is used to demonstrate the ability of SWH to image through scattering media. In a first experiment, we illuminate and image the character 'U' (see Fig. 3q) through an optically rough ground glass diffuser (220 grit). The geometry is unlike other transmission mode experiments wherein the object is illuminated directly [27] or sandwiched between two diffusers. The current choice of geometry is deliberate and designed to mimic the imaging of a target embedded in a scattering medium. Measurements were acquired for different SWLs ranging from $280\mu m$ to $2.6mm$. Figures 4b-e show four exemplary reconstructions for $\Lambda = 1.30mm$, $\Lambda = 920\mu m$, $\Lambda = 360\mu m$, and $\Lambda = 280\mu m$. In each instance, we incoherently averaged the reconstruction results for two VS positions. A comparison of the image insets in Figures 4 confirms the increased decorrelation for decreasing SWL. As discussed previously, the wavefront error for the diffuser is estimated to be $\Psi \approx 65\mu m$, and the results for $\Lambda = 280\mu m$ demonstrate performance close to the limit expressed by Eq. 2 .

In a second experiment the ground glass diffuser within the imaging path is swapped with a milky plastic plate of $\sim 4mm$ thickness. The plastic plate exhibits pronounced multiple scattering, representative of imaging through volumetric scatter. Figure 4a compares the visibility of a checkerboard viewed through the 220 grit ground glass diffuser and the plastic plate. In both cases, the checkerboard is positioned $1cm$ under the scattering plate and viewed under ambient illumination. It is evident from Figure 4a that the visibility of the checkerboard pattern is vastly diminished when viewed through the plastic plate, whereas the pattern is still visible when viewed through the diffuser.

Figure 4f-i shows reconstruction results for the same character 'U' as imaged through the plastic plate, for the same set of SWLs as the diffuser. In each instance, we incoherently averaged the reconstruction results for two VS positions. The character is reconstructed with high fidelity despite pronounced multiple scattering, suggesting the potential of SWH for imaging through volumetric scatter. A comparison of the image insets in Figures 4 confirms the diminished fidelity of imaging through volumetric scattering when compared to surface scatter.

ACKNOWLEDGEMENTS

This work was supported by DARPA through the DARPA REVEAL project (HR0011-16-C-0028), by NSF CAREER (IIS-1453192), and ONR (N00014-15-1-2735). The authors acknowledge the assistance of Mykola Kadobianskyi for making available the experimental data and supporting MATLAB scripts from [48]. The authors gratefully acknowledge the help of Zachary Lapin, Andreas Velten, Predrag Milojkovic, Gerd Häusler, Ravi Athale, and Joseph Mait in proofreading the manuscript and providing valuable comments.

Bibliography

[1] Isaac Freund. Looking through walls and around corners. *Physica A: Statistical Mechanics and its Applications*, 168(1):49 – 65, 1990. ISSN 0378-4371. doi: https://doi.org/10.1016/0378-4371(90)90357-X.

[2] L. WANG, P. P. HO, C. LIU, G. ZHANG, and R. R. ALFANO. Ballistic 2-d imaging through scattering walls using an ultrafast optical kerr gate. *Science*, 253(5021):769–771, 1991. ISSN 0036-8075. doi: 10.1126/science.253.5021.769.

[3] Seokchan Yoon, Moonseok Kim, Mooseok Jang, Youngwoon Choi, Wonjun Choi, Sungsam Kang, and Wonshik Choi. Deep optical imaging within complex scattering media. *Nature Reviews Physics*, 2(3):141–158, February 2020. doi: 10.1038/s42254-019-0143-2.

[4] Vasilis Ntziachristos. Going deeper than microscopy: the optical imaging frontier in biology. *Nature Methods*, 7, 2010.

[5] C. Dunsby and P.M.W. French. Techniques for depth-resolved imaging through turbid media including coherence-gated imaging. *J. Phys. D: Appl. Phys*, 36, 2003.

[6] Yoko Hoshi M.D. and Yukio Yamada. Overview of diffuse optical tomography and its clinical applications. *Journal of Biomedical Optics*, 21(9):1 – 11, 2016. doi: 10.1117/1.JBO.21.9.091312.

[7] K. M. Yoo and R. R. Alfano. Time-resolved coherent and incoherent components of forward light scattering in random media. *Opt. Lett.*, 15(6):320–322, Mar .

[8] Jacopo Bertolotti, Elbert Putten, Christian Blum, Ad Lagendijk, Willem Vos, and Allard Mosk. Non-invasive imaging through opaque scattering layers. *Nature*, 491:232–4, 11 2012. doi: 10.1038/nature11578.

[9] Allard Mosk, Ad Lagendijk, Geoffroy Lerosey, and Mathias Fink. Controlling waves in space and time for imaging and focusing in complex media. *Nature Photonics*, 6:283–292, 05 2012. doi: 10.1038/nphoton.2012.88.

[10] Zahid Yaqoob, Demetri Psaltis, Michael Feld, and Changhuei Yang. Optical phase conjugation for turbidity suppression in biological samples. *Nature photonics*, 2:110–115, 02 2008. doi: 10.1038/nphoton.2007.297.

[11] Ivo Micha Vellekoop, Aart Lagendijk, and Allard Mosk. Exploiting disorder for perfect focusing. *Nature photonics*, 4:320–322, 2010. ISSN 1749-4885. doi: 10.1038/nphoton.2010.3. doi:10.1038/nphoton.2010.3.

[12] Xiao Xu, Honglin Liu, and Lihong Wang. Time-reversed ultrasonically encoded optical focusing into scattering media. *Nature photonics*, 5:154, 03 2011. doi: 10.1038/nphoton.2010.306.

[13] Daniel Doktofsky, Moriya Rosenfeld, and Ori Katz. Acousto optic imaging beyond the acoustic diffraction limit using speckle decorrelation. *Communications Physics*, 3:5, 12 2020. doi: 10.1038/s42005-019-0267-9.

[14] Daniele Faccio, Andreas Velten, and Gordon Wetzstein. Non-line-of-sight imaging. *Nature Reviews Physics*, 2:318–327, 2020.

[15] M. Batarseh, S. Sukov, Z. Shen, H Gemar, R. Rezvani, and A. Dogariu. Passive sensing around the corner using spatial coherence. *Nature Communications 9, 3629 (2018)*.

[16] Matthew O'Toole, David Lindell, and Gordon Wetzstein. Confocal non-line-of-sight imaging based on the light-cone transform, Nature (2018).

[17] Xiaochun Liu, Ibon Guillen, Marco La Manna, Ji Hyun Nam, Syed Azer Reza, Toan Huu Le, Adrian Jarabo, Diego Gutierrez, and Andreas Velten. Non-line-of-sight imaging using phasor-field virtual wave optics, Nature (2019).

[18] Andreas Velten, Thomas Willwacher, Otkrist Gupta, Ashok Veeraraghavan, Moungi Bawendi, and Ramesh Raskar. Recovering three-dimensional shape around a corner using ultrafast time-of-flight imaging, Nature Communications (2012).

[19] Daniele Faccio. Non-line-of-sight imaging. *Opt. Photon. News*, 30(1):36–43, Jan 2019.

[20] Ori Katz, Pierre Heidmann, Mathias Fink, and Sylvain Gigan. Non-invasive single-shot imaging through scattering layers and around corners via speckle correlations. *Nature photonics*, 8(10):784, 2014.

[21] Ori Katz, Eran Small, and Yaron Silberberg. Looking around corners and through thin turbid layers in real time with scattered incoherent light. *Nature Photonics*, 6:549–553, 2012.

[22] David B Lindell and Gordon Wetzstein. Three-dimensional imaging through scattering media based on confocal diffuse tomography. *Nature Communications*, 11(1):1–8, 2020.

[23] Genevieve Gariepy, Francesco Tonolini, Robert Henderson, Jonathan Leach, and Daniele Faccio. Detection and tracking of moving objects hidden from view. *Nature photonics*, 10, 2016.

[24] Florian Willomitzer, Fengqiang Li, Muralidhar Madabhushi Balaji, Prasanna Rangarajan, and Oliver Cossairt. High resolution non-line-of-sight imaging with superheterodyne remote digital holography. In *Imaging and Applied Optics 2019 (COSI, IS, MATH, pcAOP)*, page CM2A.2. Optical Society of America, 2019. doi: 10.1364/COSI.2019.CM2A.2.

[25] Prasanna Rangarajan, Florian Willomitzer, Oliver Cossairt, and Marc P. Christensen. Spatially resolved indirect imaging of objects beyond the line of sight. In Jean J. Dolne, Mark F. Spencer, and Markus E. Testorf, editors, *Unconventional and Indirect Imaging, Image Reconstruction, and Wavefront Sensing 2019*, volume 11135, pages 124 – 131. International Society for Optics and Photonics, SPIE, 2019. doi: 10.1117/12.2529001.

[26] Eitan Edrei and Giuliano Scarcelli. Optical imaging through dynamic turbid media using the fourier-domain shower-curtain effect. *Optica*, 3(1):71–74, Jan 2016. doi: 10.1364/OPTICA.3.000071.

[27] Alok Kumar Singh, Dinesh N. Naik, Giancarlo Pedrini, Mitsuo Takeda, and Wolfgang Osten. Looking through a diffuser and around an opaque surface: A holographic approach. *Opt. Express*, 22(7):7694–7701, Apr 2014. doi: 10.1364/OE.22.007694.

[28] Aparna Viswanath, Prasanna Rangarajan, Duncan MacFarlane, and Marc P Christensen. Indirect imaging using correlography. In *Imaging and Applied Optics 2018 (3D, AO, AIO, COSI, DH, IS, LACSEA, LS&C, MATH, pcAOP)*, page CM2E.3. Optical Society of America, 2018. doi: 10.1364/COSI.2018.CM2E.3.

[29] Muralidhar Madabhushi Balaji, Prasanna Rangarajan, Duncan MacFarlane, Andreas Corliano, and Marc P. Christensen. Single-shot holography using scattering surfaces. In *Imaging and Applied Optics 2017 (3D, AIO, COSI, IS, MATH, pcAOP)*, page CTu2B.1. Optical Society of America, 2017. doi: 10.1364/COSI.2017.CTu2B.1.

[30] Isaac Freund, M. Rosenbluh, and Shechao Feng. Memory effects in propagation of optical waves through disordered media. *Physical review letters*, 61:2328–2331, 12 1988. doi: 10.1103/PhysRevLett.61.2328.

[31] JW. Goodman. Speckle phenomena in optics: theory and applications , Roberts and Company Publishers; 2007.

[32] Sébastien Popoff, Geoffroy Lerosey, R Carminati, Mathias Fink, and S Gigan. Measuring the transmission matrix in optics: An approach to the study and control of light propagation in disordered media. *Physical review letters*, 104:100601, 03 2010. doi: 10.1103/PhysRevLett.104.100601.

[33] Sébastien Popoff, Geoffroy Lerosey, Mathias Fink, Claude Boccara, and Sylvain Gigan. Image transmission through an opaque material. *Nature communications*, 1:81, 09 2010. doi: 10.1038/ncomms1078.

[34] Paul Sava and Erik Asphaug. Seismology on small planetary bodies by orbital laser doppler vibrometry. *Advances in Space Research*, 64(2):527 – 544, 2019. ISSN 0273-1177. doi: https://doi.org/10.1016/j.asr.2019.04.017.

[35] A. F. Fercher, H. Z. Hu, and U. Vry. Rough surface interferometry with a two-wavelength heterodyne speckle interferometer. *Appl. Opt.*, 24(14):2181–2188, Jul 1985. doi: 10.1364/AO.24.002181.

[36] U. Vry and A. F. Fercher. Higher-order statistical properties of speckle fields and their application to rough-surface interferometry. *J. Opt. Soc. Am. A*, 3(7):988–1000, Jul 1986. doi: 10.1364/JOSAA.3.000988.

[37] R. Dändliker, R. Thalmann, and D. Prongué. Two-wavelength laser interferometry using superheterodyne detection. *Opt. Lett.*, 13(5):339–341, May 1988. doi: 10.1364/OL.13.000339.

[38] Bernd Ruffing and Jürgen Fleischer. Spectral correlation of partially or fully developed speckle patterns generated by rough surfaces. *J. Opt. Soc. Am. A*, 2(10):1637–1643, Oct 1985. doi: 10.1364/JOSAA.2.001637.

[39] Aniceto Belmonte. Statistical model for fading return signals in coherent lidars. *Appl. Opt.*, 49(35):6737–6748, Dec 2010. doi: 10.1364/AO.49.006737.

[40] B. Shapiro. Large intensity fluctuations for wave propagation in random media. *Phys. Rev. Lett.*, 57:2168–2171, Oct 1986. doi: 10.1103/PhysRevLett.57.2168.

[41] A.Z. Genack and J. M. Drake. Relationship between optical intensity, fluctuations and pulse propagation in random media., EPL (Europhysics Letters) 11.4 (1990): 331.

[42] Johannes F. de Boer, Meint P. van Albada, and Ad Lagendijk. Transmission and intensity correlations in wave propagation through random media. *Phys. Rev. B*, 45:658–666, Jan 1992. doi: 10.1103/PhysRevB.45.658.

[43] Eric Akkermans and Gilles Montambaux. *Mesoscopic Physics of Electrons and Photons*. Cambridge University Press, 2007. doi: 10.1017/CBO9780511618833.

[44] Alesya Mikhailovskaya, Julien Fade, and Jerome Crassous. Speckle decorrelation with wavelength shift as a simple way to image transport mean free path, The European Physical Journal Applied Physics 85.3 (2019): 30701.

[45] Charles A. Thompson, Kevin J. Webb, and Andrew M. Weiner. Diffusive media characterization with laser speckle. *Appl. Opt.*, 36(16):3726–3734, Jun 1997. doi: 10.1364/AO.36.003726.

[46] MP Van Albada, JF De Boer, and A Lagendijk. Observation of long-range intensity correlation in the transport of coherent light through a random medium. *Physical review letters*, 64 (23):2787, 1990.

[47] Beer. Bestimmung der absorption des rothen lichts in farbigen flüssigkeiten. *Annalen der Physik*, 162(5):78–88, 1852. doi: 10.1002/andp.18521620505.

[48] Mykola Kadobianskyi, Ioannis N Papadopoulos, Thomas Chaigne, Roarke Horstmeyer, and Benjamin Judkewitz. Scattering correlations of time-gated light. *Optica*, 5(4):389–394, 2018.

[49] Maciej Wojtkowski. High-speed optical coherence tomography: basics and applications. *Appl. Opt.*, 49(16):D30–D61, Jun 2010. doi: 10.1364/AO.49.000D30.

[50] Peter Andretzky, Michael W. Lindner, Juergen M. Herrmann, A. Schultz, M. Konzog, F. Kiesewetter, and Gerd Haeusler. Optical coherence tomography by spectral radar: dynamic range estimation and in-vivo measurements of skin. In Marco Dal Fante, Hans-Jochen Foth, Neville Krasner M.D., Renato Marchesini, and Halina Podbielska M.D., editors, *Optical and Imaging Techniques for Biomonitoring IV*, volume 3567, pages 78 – 87. International Society for Optics and Photonics, SPIE, 1999. doi: 10.1117/12.339173.

[51] A F Fercher and E Roth. Ophthalmic Laser Interferometry. In Gerhard J. Mueller, editor, *Optical Instrumentation for Biomedical Laser Applications*, volume 0658, pages 48 – 51. International Society for Optics and Photonics, SPIE, 1986. doi: 10.1117/12.938523.

[52] D Huang, EA Swanson, CP Lin, JS Schuman, WG Stinson, W Chang, MR Hee, T Flotte, K Gregory, CA Puliafito, and al. et. Optical coherence tomography. *Science*, 254(5035): 1178–1181, 1991. ISSN 0036-8075. doi: 10.1126/science.1957169.

[53] E. N. Leith and G. J. Swanson. Achromatic interferometers for white light optical processing and holography. *Appl. Opt.*, 19(4):638–644, Feb 1980. doi: 10.1364/AO.19.000638.

[54] Thomas Dresel, Gerd Häusler, and Holger Venzke. Three-dimensional sensing of rough surfaces by coherence radar. *Appl. Opt.*, 31(7):919–925, Mar 1992. doi: 10.1364/AO.31.000919.

[55] Jun Ye. Absolute measurement of a long, arbitrary distance to less than an optical fringe. *Opt. Lett.*, 29(10):1153–1155, May 2004. doi: 10.1364/OL.29.001153.

[56] Seung-Woo Kim. Metrology: combs rule, Nature photonics 3.6 (2009): 313.

[57] Jonghan Jin. Dimensional metrology using the optical comb of a mode-locked laser, Measurement Science and Technology 27.2 (2015): 022001.

[58] Lord Rayleigh, Philos. Mag. 8, 403 (1879). Reprinted in his Scientific Papers (Cambridge U. Press, 1899), Vol. 1, pp. 432-435.

[59] Jesse Zheng. *Optical frequency-modulated continuous-wave (FMCW) interferometry*, volume 107. Springer Science & Business Media, 2005.

[60] Yan Liu, Cheng Ma, Yuecheng Shen, and Lihong V. Wang. Bit-efficient, sub-millisecond wavefront measurement using a lock-in camera for time-reversal based optical focusing inside scattering media. *Opt. Lett.*, 41(7):1321–1324, Apr 2016. doi: 10.1364/OL.41.001321.

[61] Heliotis. Helicam C3 , https://www.heliotis.ch/html/lockInCameraC3.htm).

Figures

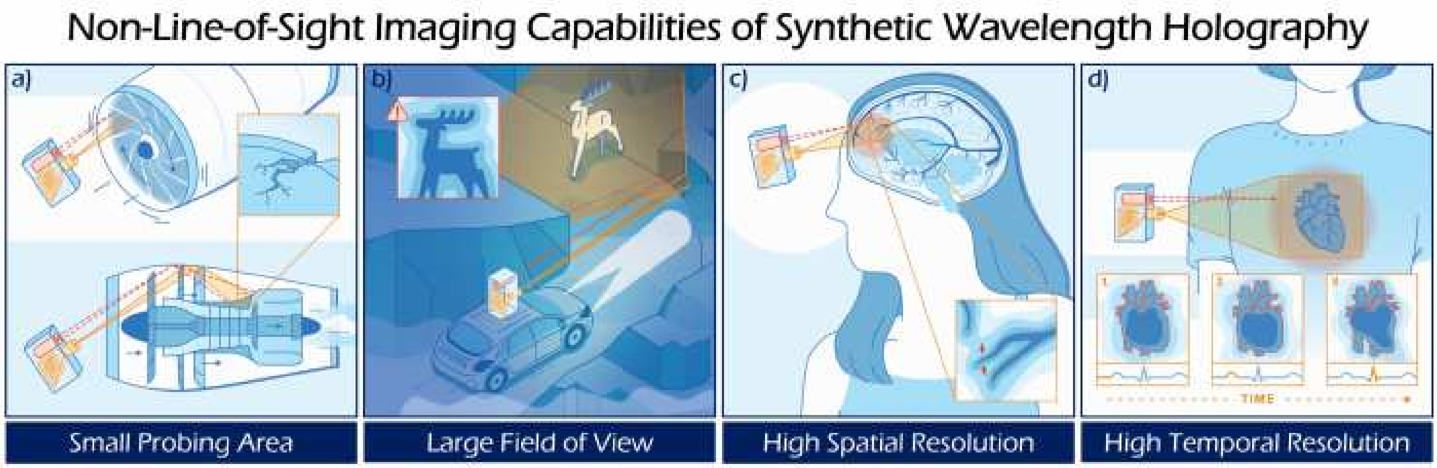

Figure 1

Imaging objects obscured from direct view using 'Synthetic Wavelength Holography'(SWL). The approach combines four key attributes highlighted in the following NLoS application scenarios: In each example, a scattering surface or medium is used to indirectly illuminate, and intercept light scattered by the hidden objects. a) A small probing area allows to inspect defects in tightly confined spaces, e.g., in running aircraft engines. b) A large FoV allows to measure/detect hidden objects without previous knowledge of their position as, e.g., important when navigating in degraded visual environments. c) High spatial resolution allows for the measurement of small structures, such as non-invasive imaging of brain vessels through the skull. d) High temporal resolution allows to image objects in motion, e.g., to discern cardiac arrhythmia through the chest. The combination of these attributes in a single approach is unprecedented in the current state of the art.

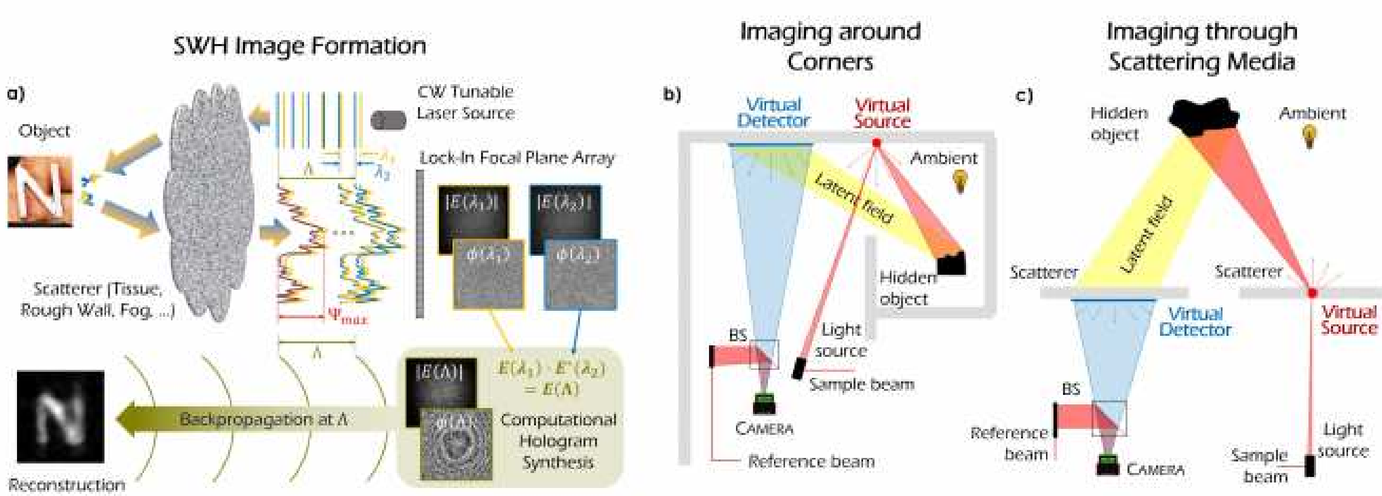

Figure 2

[Please see the manuscript file to view this figure caption.]

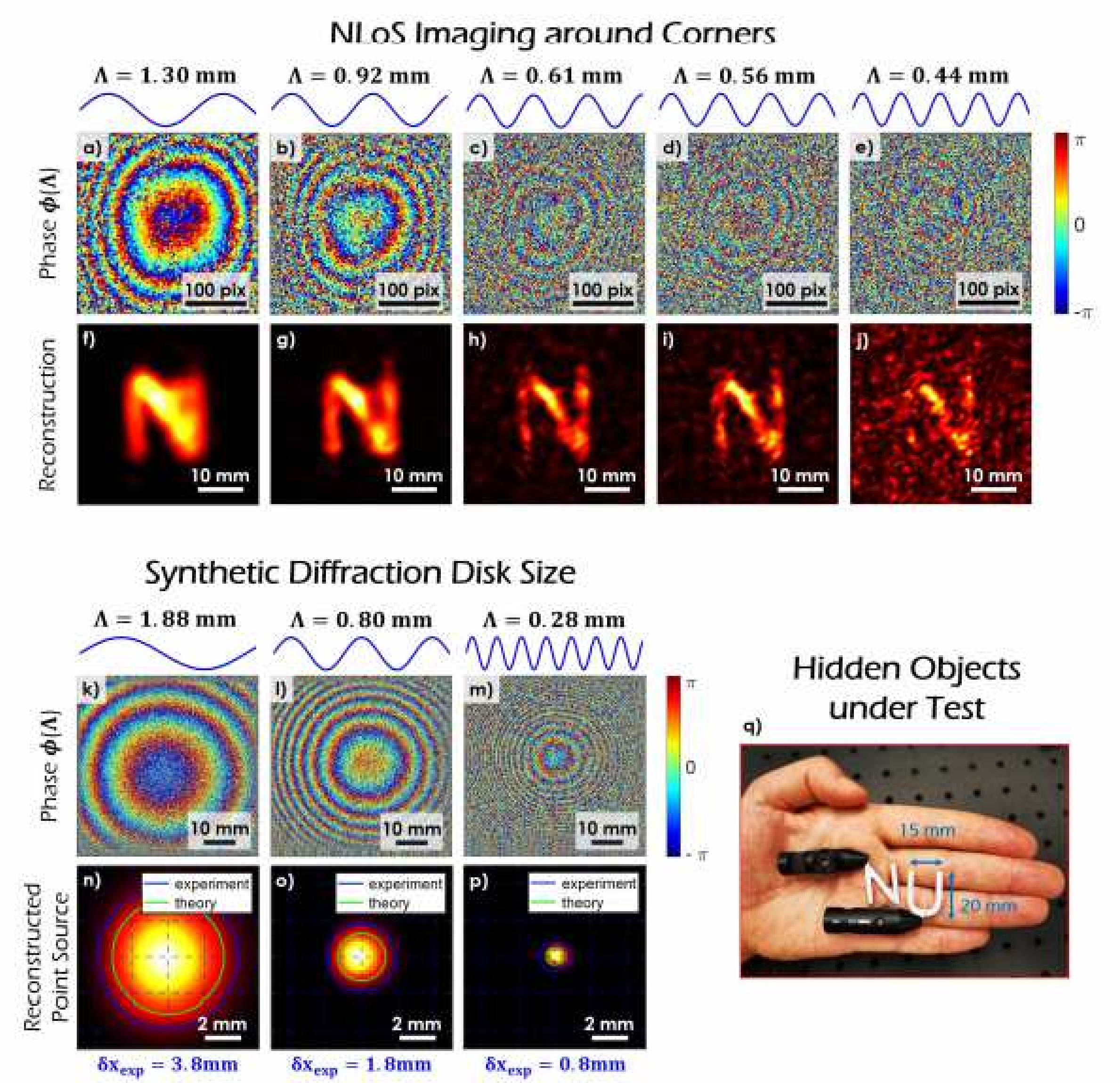

Figure 3

Experimental results for imaging around corners with SWH. a)-j) Imaging the character 'N' (15mm×20mm) at five different SWLs. a)-e) The phase of the synthetic holograms at the VD surface. f)-j) Respective reconstructions. The resolution of the reconstructions increases with decreasing SWL. However, the speckle-artifacts increase due to the decorrelation of the two optical fields at λ1 and λ2. k)-p) Reconstruction of an obscured point source for three different SWLs. k)-m) Phase of the synthetic holograms at the VD surface. n)-p) Reconstruction of the 'synthetic diffraction disc'. As in classical optics, the disc size varies linearly with the wavelength (in this case the SWL). The experimental value is close to the theoretical expectation. For p), the point source is reconstructed with sub-mm precision. q) Image of the targets used in the experiments of this paper: Two characters 'N' and 'U' with dimensions 15mm×20mm (plus black mountings).

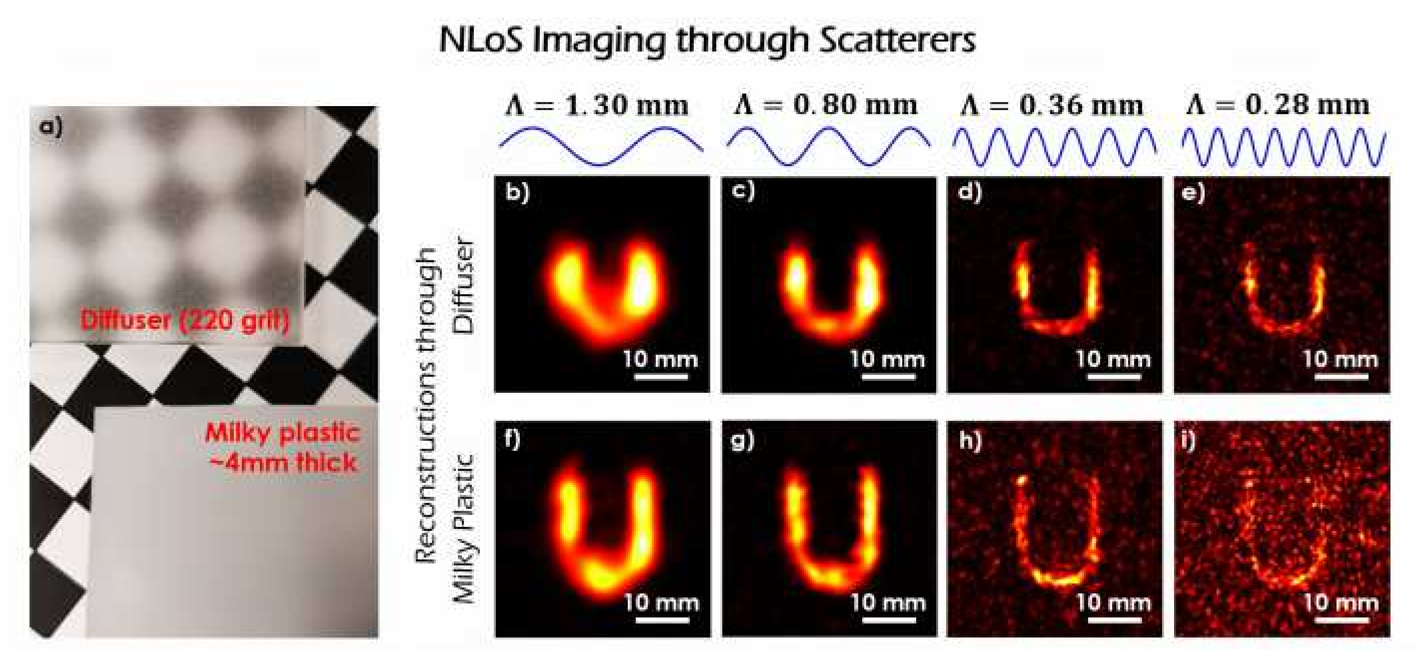

Figure 4

Experimental results for imaging through scattering media with SWH. A schematic of the experimental setup is available in Fig. 2c. a) Scatterers obscuring the object: A 220 grit ground glass diffuser and a milky white plastic plate of ~ 4mm thickness, both placed ~ 1cm over a checker pattern to demonstrate the degradation in visibility. b)-e) Reconstructions of measurements taken through the ground glass diffuser. f)-i) Reconstructions of measurements taken through the milky plastic plate. The character can be reconstructed with impressive quality. The larger OPD in the plastic plate leads to greater decorrelation if the SWL is decreased

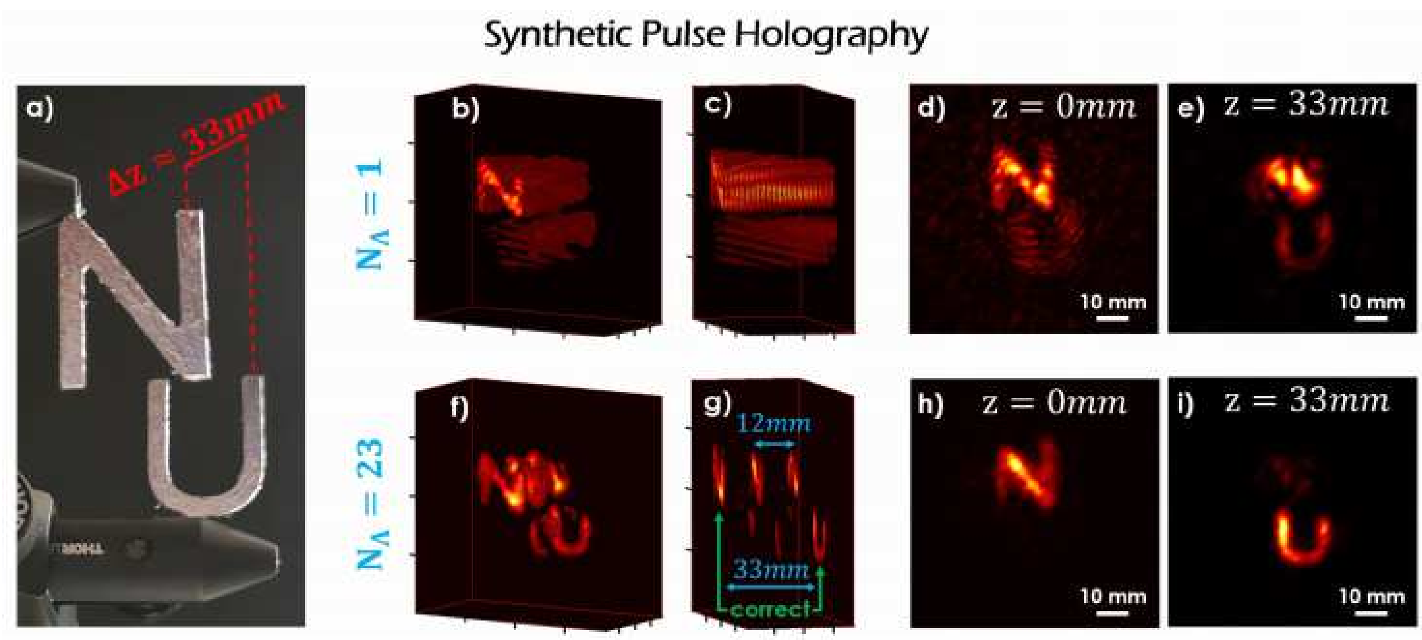

Figure 5

Experimental Results for the generation of a 'synthetic pulse train' with SHW. a) Target, consisting of two characters with a longitudinal separation of 33mm. b)-e) Reconstruction of the characters, using only NΛ = 1 SWL (Λ = 0.8mm). Due to the properties of holographic backpropagation, a separation of the characters in depth is not possible. f)-i) Reconstruction, calculated from coherent superposition of the backpropagated fields at NΛ = 23 SWLs. Letters are separable. The pulse distance of the synthesized pulse train can be seen in (f) and (g).

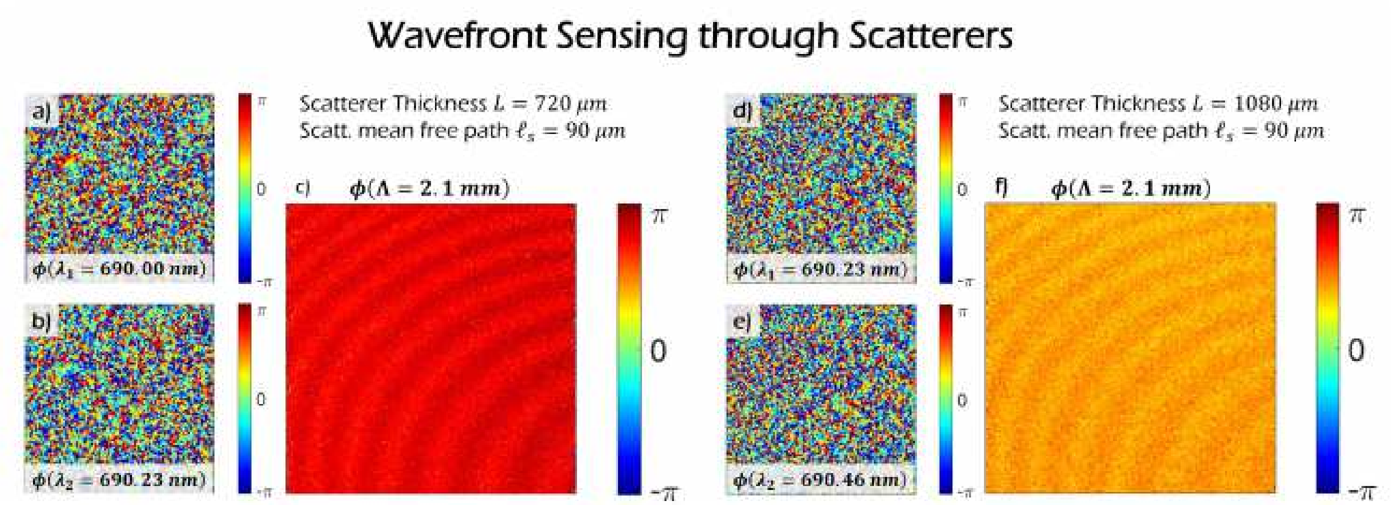

Figure 6

[Please see the manuscript file to view this figure caption.]

Supplementary Files

This is a list of supplementary files associated with this preprint. Click to download.

- SupplementaryMaterialSWHWillomitzer20200928.pdf